

# Controlling the Error on Target Motion through Real-time Mesh Adaptation: Applications to Deep Brain Stimulation

Huu Phuoc Bui<sup>1,\*</sup>, Satyendra Tomar<sup>1</sup>, Hadrien Courtecuisse<sup>2</sup>, Michel Audette<sup>3</sup>, Stéphane Cotin<sup>4</sup> and Stéphane P. A Bordas<sup>1,5,6,\*</sup>

<sup>1</sup>*Institute of Computational Engineering, University of Luxembourg, Faculty of Sciences Communication and Technology, Luxembourg*

<sup>2</sup>*University of Strasbourg, CNRS, ICube, Strasbourg, France*

<sup>3</sup>*Department of Modeling, Simulation and Visualization Engineering, Old Dominion University, Norfolk, USA*

<sup>4</sup>*Inria Nancy-Grand Est, Villers-lès-Nancy, France*

<sup>5</sup>*Institute of Mechanics and Advanced Materials, School of Engineering, Cardiff University, UK*

<sup>6</sup>*Intelligent Systems for Medicine Laboratory, University of Western Australia, Perth, Australia*

Correspondence\*:

Stéphane P. A. Bordas and Huu Phuoc Bui

stephane.bordas@alum.northwestern.edu, huu-phuoc.bui@insa-alumni-lyon.org

## ABSTRACT

We present an error-controlled mesh refinement procedure for needle insertion simulation and apply it to the simulation of electrode implantation for deep brain stimulation, including brain shift.

Our approach enables to control the error in the computation of the displacement and stress fields around the needle tip and needle shaft by suitably refining the mesh, whilst maintaining a coarser mesh in other parts of the domain.

We demonstrate through academic and practical examples that our approach increases the accuracy of the displacement and stress fields around the needle without increasing the computational expense. This enables real-time simulations.

The proposed methodology has direct implications to increase the accuracy and control the computational expense of the simulation of percutaneous procedures such as biopsy, brachytherapy, regional anesthesia, or cryotherapy and can be essential to the development of robotic guidance.

**Keywords:** finite element method, real-time error estimate, adaptive refinement, deep brain stimulation, adaptivity, brain shift

## 1 INTRODUCTION

Real-time simulations are increasingly common for various applications, from geometric design (Nealen et al., 2006; Wang et al., 2015) to medical simulation (Courtecuisse et al., 2014). Within the medical

context, simulations that involve the interaction of a surgeon or an interventional radiologist dealing with soft, deformable organs. These simulations do not only have the potential to help surgeons train or plan complex operations but they can also guide them during the intervention itself. In spite of the obvious importance of quality control in such safety-critical advanced numerical tools, no approach is known to evaluate and control the error committed by simulations. If this were possible, not only would the user be provided with useful information regarding the quality of the results, but the computational cost could be focused on where the error is large and decreased where it is small, thus leading to computational savings.

Yet, whilst the literature in error estimation is rich within the computational mechanics community, little or no work has been done in the context of medical simulation, in particular for real-time applications (Wu et al., 2001). The error in numerical simulation comes in three guises. First, the user writes a mathematical model of the system of interest. For example, they may choose a corotational model to represent the tissue, or a hyper-elastic model with a number of parameters. The inability of the model to represent the physical reality is measured by the *model error*.

Second, the mathematical model must be solved numerically, since analytical solutions are rarely available. For example, a user might wish to use the finite element method (FEM), or meshfree methods, or the boundary element method. The inability of a numerical method to exactly solve the mathematical model leads to the *discretisation error*.

Third, the set of linear equations provided by the discretised model must be solved numerically. The associated error is known as the *numerical error* and incorporates, e.g. round-off errors.

In this paper, we tackle only discretisation error. Our assumption is that the mathematical model used (here the corotational formulation), properly represents the behaviour of the organ in question, in our case the brain. This is a strong assumption which is most likely not verified in general, as it was shown that brain matter behaves hyper-visco-elastically (Mihai et al., 2015).

Yet, the tools we develop in this paper are directly applicable to any model which can be described in the form of partial differential equations, which is the case of most models of soft tissues. The aim of this paper is therefore to demonstrate that error estimation techniques can be effectively used, even in real-time scenario, to control the discretisation error and drive local refinement of the discretisation. We focus on the problem of needle insertion because of the particular challenges it poses, due to the localisation of deformations and stresses close to the needle shaft.

Thanks to their minimally invasive character, needle-based percutaneous procedures are an important part of modern clinical interventions such as biopsy, brachytherapy, cryotherapy, regional anesthesia, or drug delivery. The success of these procedures depends on good training and careful planning to optimise the path to the target, while avoiding critical internal structures (Hamzé et al., 2016). In some instances, the procedure can also be assisted by robotic devices (Elgezua et al., 2013). Unfortunately, natural tissue motion before or during the intervention, and deformation due to needle insertion generally lead to incorrect or inefficient planning (Hamzé et al., 2016). An accurate simulation of needle insertion can address these issues, possibly in a manner complemented by imaging in intraoperative scenarios. For most problems, computational speed is vital, since the biomechanical simulation is at the core of an optimisation algorithm for the needle path or for a robotic control loop.

In needle insertion simulations, one has to deal with three main models: a soft tissue model, a flexible needle model, and a needle-tissue interaction model. Needle and tissue models can rely on linear or non-linear constitutive laws (see the survey in Abolhassani et al. (2007)). A nonlinear viscoelastic Kelvin model is used for the needle in Mahvash and Dupont (2009). The interaction model between the needle and

the tissue remains a major challenge. It consists of different physical phenomena, such as frictional contact on tissue surface, puncturing, cutting, sliding with friction, and the Poynting effect. Dehghan et al. (2008) propose an ultrasound-based motion estimation to model needle-tissue interaction. To avoid obstacles while steering the needle during insertion, different kind of needles have been proposed, for example, a symmetric tip (Heverly et al., 2005), a flexible bevel tip (Alterovitz et al., 2005; Webster et al., 2006; Misra et al., 2010), as well as a compliant needle model (Tang et al., 2008).

FEM is the most commonly used numerical method for needle insertion simulations, see e.g. DiMaio and Salcudean (2003), Hing et al. (2006), Jiang et al. (2008). In order to numerically solve the equilibrium equations of mathematical models, FEM uses the concept of discretisation, in which the volume of an object/organ is decomposed into elements (such as tetrahedra or hexahedra). The arrangement of these elements defines the mesh, and the continuous mathematical problem, in this case biomechanical deformation, can be established on this mesh. The resulting discrete problem (refer to Section 2.2), with the number of unknowns directly proportional to the number of elements in the mesh, can then be easily solved on a computer. It is noted that the computational cost (time) is also directly proportional (with cubic power) to the number of unknowns, i.e., the CPU time is of the order of  $N^3$ , where  $N$  denotes the number of unknowns of the problem (Watkins, 2005).

Using a uniform coarse mesh (involving few elements of the same shape) is undermined by the limitation that discontinuities engendered by cuts, singularities or stress concentrations can not be captured. On the other hand, it is usually uneconomical, or prohibitively expensive, to use a uniformly fine mesh (involving same shaped elements but many more as compared to a coarse mesh). Therefore, in the context of real-time simulations, an economical hybrid mesh should be used to deliver fast simulation response while still enabling accurate simulation results.

Our aim is to model needle-tissue interactions using an adaptive meshing strategy, which is driven by an a posteriori error estimation. An a posteriori error estimation approach obtains the actual error bounds using the computed solution (instead of the asymptotic bounds on the solution of the original mathematical problem). In this paper we use an a posteriori error estimation technique called super-convergent patch recovery (SPR). The SPR technique was proposed by Zienkiewicz and Zhu (1992), and its asymptotic convergence is studied in Carstensen and Bartels (2002), Bartels and Carstensen (2002). By solving the discrete problem on a computer, we obtain the numerical solution (henceforth called the *raw* solution as in Bordas et al. (2008)). In SPR (see Section 2.3 for details), we post-process the *raw* solution to obtain an *improved* solution, to which the *raw* solution is compared. Where the difference between the *raw* solution and the *improved* solution is above a certain threshold, the error level is high and the mesh should be refined, and where these two solutions are close together, the mesh can be kept unchanged or coarsened. Note that the mesh refinement is only introduced as a means to improve the accuracy of the needle-tissue interactions. Similar to the approach used in Duriez et al. (2009), we do not require the mesh used for the tissue to conform to the needle path.

The efficiency of our method will be studied through a heuristic needle insertion scenario, and also through a more complex simulation of the insertion of an electrode lead. Deep Brain Stimulation (DBS) is a surgical procedure used to treat a variety of disabling neurological symptoms, such as Parkinson's disease (PD). DBS consists of inserting a long needle-shaped electrode (or electrode lead) through a small opening in the skull into the brain to reach the target area which for PD is the subthalamic nucleus (STN). Subsequently, a neurostimulator sends therapeutic electrical impulses to this target implanted with electrodes. The success of the therapy largely depends on the precise implantation of the stimulation electrode (Breit et al., 2004), although increasingly, DBS targeting benefits from knowledge of afferent

and efferent white matter tracts (Calabrese, 2016). This procedure necessitates a pre-operative planning step for determining the target coordinates to implant the electrodes, as well as a trajectory to deliver the insertion cannula, through which then one determines the electrode insertion path. A pre-operative magnetic resonance imaging (MRI) of the patient is employed to identify and locate the target within the brain. However, during the DBS procedure, as a burr hole is drilled in the skull to access the brain tissue, brain shift occurs due to the leak of cerebro-spinal fluid (Bilger et al., 2011; Hamzé et al., 2015). This includes an error in the planning, that can at best make the therapy ineffective, and at worst cause complications, such as psychiatric complications (Piasecki and Jefferson, 2004). Therefore, brain shift prior to electrode insertion will be taken into account in our simulations.

The remaining of the paper is organised as follows. Section 2 describes the problem being solved. The interaction model between needle and tissue is formulated, and it is described how the elements are marked for refinement during simulation by employing an error estimate. It is then followed by the discussion on solving the system equations with constraints. Numerical results are presented in Section 3, which shows the efficiency of the proposed approach through a simple needle insertion scenario, as well as through more complex DBS lead insertion simulation. Finally, conclusions are drawn in Section 4.

## 2 METHODS

We first outline the mathematical model we choose to represent the brain and its interaction with the cannula/needle/lead. We then describe the approach we follow to solve this problem numerically.

We use corotational elasticity, which implicitly assumes that the deformations of the brain are small. We develop a needle/tissue interaction model based on friction. The problem is solved using hexahedron-based finite elements within the open-source Simulation Open Framework Architecture (SOFA, [www.sofa-framework.org](http://www.sofa-framework.org)). The local  $h$ -refinement strategy is based upon simple SPR-based a posteriori error estimation method.

### 2.1 Problem statement

Within the context of needle (or cannula/lead) insertion into soft tissue, both the needle and the tissue are modeled as dynamic deformable objects. Let  $\Omega$  represent the volume of an object (e.g. the tissue). Undergoing external force  $\bar{\mathbf{t}}$ , which is applied on the boundary part  $\Gamma_t$  on the object boundary  $\Gamma$ , and bearing a prescribed displacement  $\bar{\mathbf{u}}$  on its boundary part  $\Gamma_u$  in  $\Gamma$ , see Fig. 1, the dynamic equilibrium motion equation of the object is expressed by (Zienkiewicz and Taylor, 2000; Liu and Quek, 2014)

$$\text{div } \boldsymbol{\sigma} + \mathbf{b} + \boldsymbol{\lambda} = \rho \ddot{\mathbf{u}} \quad \text{in } \Omega. \quad (1)$$

Here  $\boldsymbol{\sigma}$  is the Cauchy stress tensor (accounting for internal forces),  $\mathbf{b}$  is the body force vector (e.g. gravity),  $\boldsymbol{\lambda}$  is the interaction force with another object (e.g. a needle),  $\rho$  is the mass density,  $\mathbf{u}$  is the displacement field of the object, and  $\ddot{x}$  is the second partial derivative of  $x$  with respect to time. In physical terms, the divergence term ( $\text{div } \boldsymbol{\sigma}$ ) is the sum of the derivatives of the stress tensor components with respect to each axis direction. The compatibility conditions on the boundaries  $\Gamma_t$  and  $\Gamma_u$  read

$$\boldsymbol{\sigma} \cdot \mathbf{n} = \bar{\mathbf{t}} \quad \text{on } \Gamma_t \quad (2a)$$

$$\mathbf{u} = \bar{\mathbf{u}} \quad \text{on } \Gamma_u. \quad (2b)$$

Eqs. (2a) and (2b) are known as Neumann and Dirichlet boundary conditions, respectively.

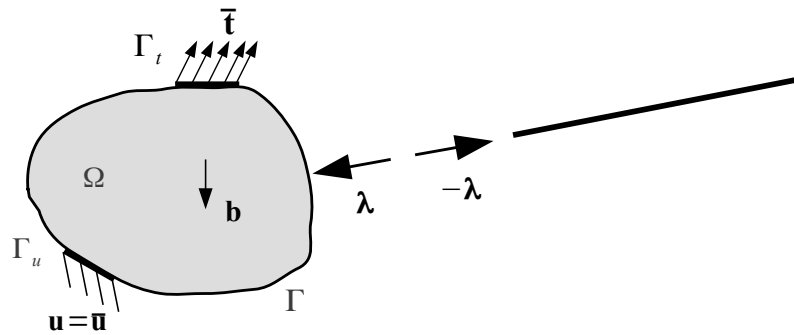


**Figure 1.** A body  $\Omega$  subjected to a traction  $\bar{\mathbf{t}}$ , a body force  $\mathbf{b}$ , an prescribed displacement  $\bar{\mathbf{u}}$ , and is in interaction with another object through interaction forces  $\boldsymbol{\lambda}$ .

The strain in the object, which is a measure of the object deformation, can be expressed from the gradient of the displacement as

$$\boldsymbol{\epsilon} = \frac{1}{2} \left( \text{grad } \mathbf{u} + (\text{grad } \mathbf{u})^T \right). \quad (3)$$

The constitutive law, that expresses the relation between stress and strain tensors (through a function  $f$ ) of the object via the model internal (intrinsic) variables  $\boldsymbol{\nu} = (\nu_1, \nu_2, \dots, \nu_n)$ , reads

$$\boldsymbol{\sigma} = f(\boldsymbol{\epsilon}, \boldsymbol{\nu}). \quad (4)$$

Eqs. (1) to (4) constitute the governing equations that describe the behaviour of the object in the sense of continuum mechanics.

The interaction force  $\boldsymbol{\lambda}$  is defined from the interaction law between the needle and the tissue. During the needle insertion, three types of constraints between the needle and the tissue are prescribed, see Fig. 2. Coulomb's friction law is used to describe frictional contact within these three types of constraints. First, a

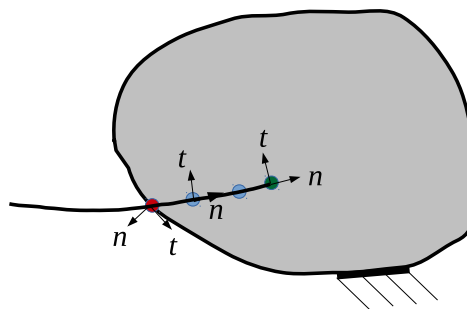


**Figure 2.** Three types of constraints between the needle and soft tissue: surface puncture (in red, denoted by  $\lambda^{ts}$ ), needle tip constraint (in green, denoted by  $\lambda^{nt}$ ) and needle shaft constraints (in blue, denoted by  $\lambda^{ns}$ ). A local coordinate system  $n$ - $t$  is defined at each constraint point.

puncture constraint is defined between the needle tip and the tissue surface. This constraint satisfies the Kuhn-Tucker conditions. The latter expresses that the contact force only exists when the needle tip is in contact with the tissue surface. In the direction  $n$  (normal to the tissue surface), this condition reads

$$\delta_n \geq 0, \quad \lambda_n^{ts} \geq 0, \quad \delta_n \cdot \lambda_n^{ts} = 0, \quad (5)$$

where, the superscript  $ts$  stands for the constraints on the tissue surface,  $\delta_n$  denotes the distance between the needle tip and the tissue surface in the direction  $n$ , and  $\lambda_n^{ts}$  denotes the contact force in that direction. Let  $\lambda_{p0}$  represent the puncture strength of the tissue. When the contact force is higher than a threshold (puncture strength of the tissue)

$$\lambda_n^{ts} > \lambda_{p0}, \quad (6)$$

the needle can penetrate into the tissue. When the needle tip has not penetrated into the tissue surface yet, the relative motion between them can be described by a friction law. In the tangential direction  $t$ , represented by the subscript  $\cdot_t$ . Coulomb's friction is considered in order to take into account the stick/slip between the needle tip and tissue surface

$$\lambda_t^{ts} < \mu \lambda_n^{ts} \quad (\text{stick}); \quad \lambda_t^{ts} = \mu \lambda_n^{ts} \quad (\text{slip}), \quad (7)$$

where  $\mu$  denotes the friction parameter.

Second, a needle tip constraint is defined as soon as the tip penetrates into the tissue. Depending on the relationship between the contact forces in the normal direction  $n$  (along the needle shaft) and in the tangent direction  $t$  (see Fig. 2), the needle tip can cut and go through the tissue or not

$$\lambda_n^{nt} < \mu \lambda_t^{nt} + \lambda_{c0} \quad (\text{stick}); \quad \lambda_n^{nt} \geq \mu \lambda_t^{nt} + \lambda_{c0} \quad (\text{cut and slip}), \quad (8)$$

where, the superscript  $nt$  stands for the constraints at the needle tip, and  $\lambda_{c0}$  denotes the cutting strength of the tissue.

Finally, needle shaft constraints (denoted by superscript  $ns$ ) are defined along the needle shaft so that the needle shaft is enforced to follow the insertion trajectory created by the advancing needle tip. Again, the Coulomb's friction law is applied to these constraints to represent the stick and slide contacts between the tissue and the needle shaft

$$\lambda_n^{ns} < \mu \lambda_t^{ns} \quad (\text{stick}); \quad \lambda_n^{ns} = \mu \lambda_t^{ns} \quad (\text{slide}). \quad (9)$$

Note that these three types of constraints describe different kinds of physical interactions between the needle and the tissue. However, we depict three of them as interaction constraint vector, collectively denoted by  $\lambda$  in the following, which can be solved numerically.

## 2.2 Weak form

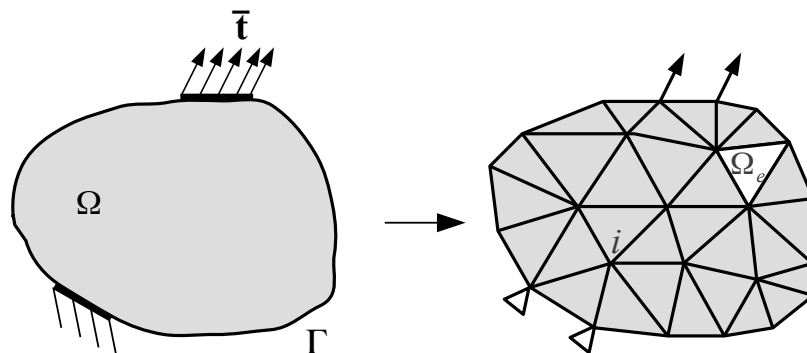


**Figure 3.** Simplified illustration of FEM discretisation in two dimensions.

Since the partial differential equation (1), which states the equilibrium of the system, involves both spatial and temporal derivatives, it can be solved numerically by discretising that equation in both space (the volume representing the object) and time.

Using  $N_n$  nodes, the domain  $\Omega$ , which represents tissue or needle, is spatially discretised into  $N_e$  finite elements  $\Omega_e$ ,  $e = 1, 2, \dots, N_e$ , see Figure 3. By integrating the equilibrium equation on each element volume, and assembling for the whole volume, we obtain the discrete problem as (see, e.g., Liu and Quek (2014), Zienkiewicz and Taylor (2000))

$$\mathbf{M}\ddot{\mathbf{u}} + \mathbf{C}\dot{\mathbf{u}} + \mathbf{K}\mathbf{u} = \mathbf{f}^{ext} + \mathbf{H}^T\boldsymbol{\lambda}, \quad (10)$$

where  $\mathbf{M}$  is the mass matrix,  $\mathbf{K}$  is the stiffness matrix,  $\mathbf{C}$  is the damping matrix, and  $\mathbf{f}^{ext}$  is the external force vector. The interaction force constraints  $\boldsymbol{\lambda}$ , between the needle and the tissue, are computed using Lagrange multipliers (in numerical methods, the constraints  $\boldsymbol{\lambda}$  are called Lagrange multipliers, and thus we use the same notation), where  $\mathbf{H}^T$  provides the direction of the constraints.

Eq. (10) can be rewritten as

$$\mathbf{M}\mathbf{a} = \mathbf{f}(\mathbf{x}, \mathbf{v}) + \mathbf{H}^T\boldsymbol{\lambda}, \quad (11)$$

where  $\mathbf{a} = \ddot{\mathbf{u}}$ ,  $\mathbf{x}$ ,  $\mathbf{v} = \dot{\mathbf{u}}$  are the acceleration, position and velocity vectors, respectively, and  $\mathbf{f}(\mathbf{x}, \mathbf{v}) = \mathbf{f}^{ext} - \mathbf{K}\mathbf{u} - \mathbf{C}\mathbf{v}$  represents the net force (the difference of the external and internal forces) applied to the object. Note that the displacement vector  $\mathbf{u}$  is expressed through the current and initial position vectors,  $\mathbf{x}$  and  $\mathbf{x}_0$ , respectively, as  $\mathbf{u} = \mathbf{x} - \mathbf{x}_0$ .

For temporal discretisation, i.e. to numerically solve the problem in time, we use an implicit backward Euler scheme (Baraff and Witkin, 1998), which is described as follows

$$\dot{\mathbf{u}}_{t+\tau} = \dot{\mathbf{u}}_t + \tau\ddot{\mathbf{u}}_{t+\tau}; \quad \mathbf{u}_{t+\tau} = \mathbf{u}_t + \tau\dot{\mathbf{u}}_{t+\tau}, \quad (12)$$

where  $\tau$  denotes the time step. Inserting Eq. (12) into Eq. (11) yields the final discrete system

$$\underbrace{(\mathbf{M} - \tau\mathbf{C} - \tau^2\mathbf{K})}_{\mathbf{A}} d\mathbf{v} = \underbrace{\tau\mathbf{f}(\mathbf{x}^t, \mathbf{v}^t) + \tau^2\mathbf{K}\mathbf{v}^t}_{\mathbf{b}} + \mathbf{H}^T\boldsymbol{\lambda} \quad (13)$$

or simply  $\mathbf{A}d\mathbf{v} = \mathbf{b} + \mathbf{H}^T\boldsymbol{\lambda}$ , where  $d\mathbf{v} = \mathbf{v}_{t+\tau} - \mathbf{v}_t$ . After solving (13) for  $d\mathbf{v}$ , the position and velocity are updated for needle and tissue as

$$\mathbf{v}_{t+\tau} = d\mathbf{v} + \mathbf{v}_t; \quad \mathbf{x}_{t+\tau} = \mathbf{x}_t + \tau\mathbf{v}_{t+\tau}. \quad (14)$$

In this contribution, a lumped mass matrix, in which a diagonal mass matrix (from the mass density  $\rho$ ) is integrated over the volume of each element is employed. The stiffness matrix  $\mathbf{K}$  is computed based on the corotational FEM, in which the rigid body motion from total finite element displacements is extracted (since it does not contribute to element deformations, see Felippa and Haugen (2005)). Note that the corotational FEM formulation makes it possible to handle large rotations for both, needle as well as tissue. For higher accuracy of the computed strain field, the soft tissue domain is discretised using hexahedral elements<sup>1</sup>. To avoid the complex issue of generating an exact hexahedral mesh of the domain, we use a mesh that does not conform to the boundary of the domain, similar to the approach of Immersed Boundary

<sup>1</sup> It is also possible to use smoothed tetrahedral elements, which do not lock, see, e.g. Nguyen-Xuan et al. (2010), Lee et al. (2017), Mendizabal et al. (2017).



Method (Pinelli et al., 2010) or unfitted finite elements (Belytschko et al., 2003; Burman et al., 2015). The needle, on the other hand, is modeled using serially-linked beam elements. In this case, each node of the needle has 6 degrees of freedom (3 translations and 3 rotations), while the tissue model uses only 3 translational degrees of freedom per node.

### 2.3 Error estimate and adaptive refinement

There are a number of factors involved in the accuracy of the outcome of surgical simulators. They can mainly be divided into two sources: modelling error and discretisation error. The first error source arises when a mathematical model is formulated for a physical problem, prompting the question: does the resulting model correctly describe the physical phenomenon? The second error source comes from the discretisation approach used by numerical methods such as the Finite Element (FE) method (Zienkiewicz et al., 2013), or meshfree methods (Nguyen et al., 2008; Griebel and Schweitzer, 2003) to solve the mathematical model. In this paper, we assume the mathematical model to be correctly representing reality and focus on the discretisation error.

Since the FE formulation is based on the discretisation of the physical domain, it introduces a discretisation error in the result. We estimate this error source by the superconvergent patch recovery (SPR) procedure (Zienkiewicz and Zhu, 1992). This information is then used to adaptively refine elements where the error is high.

The SPR is based on the following simple idea. The displacement field is obtained from solving the equilibrium equation, and the stress field is then computed by differentiating the polynomial approximation of the displacement field. In doing so, one loses numerical accuracy of the stress field (the differentiation reduces the polynomial degree by one). The stress field, obtained by the FEM, is possibly discontinuous across element boundaries. However, assuming that the original problem of the continuum has a smooth (continuous) solution, one can post-process the FEM solution to obtain higher accuracy. This post-processing is done on a collection of neighboring elements, which is called a patch. Using SPR, the post-processed (smoothed) stress field  $\sigma^s$  is recovered from the stresses computed at the element centre. The idea of this technique is based on the fact that the stress and strain are more accurate at the superconvergent points (for the case of linear hexahedral elements used in this study, these points are at the centre point of elements), than anywhere else in the element. Using the least squares approach, the values of stress and strain at the superconvergent points are then employed to recover the nodal stress and strain.

We define the approximate error of an element  $\Omega_e$  as

$$\eta_e = \sqrt{\int_{\Omega_e} (\epsilon^h - \epsilon^s)^T (\sigma^h - \sigma^s) d\Omega}, \quad (15)$$

which is the energy norm of the distance between the FEM solution, denoted by superscript  $h$ , and an improved (recovered) solution, denoted by superscript  $s$ . We mark an element for refinement if

$$\eta_e \geq \theta \eta_M, \quad 0 < \theta < 1, \quad \text{where } \eta_M = \max_e \eta_e. \quad (16)$$

Once an element is marked for refinement, the element is replaced by several elements according to a predefined template. The template is simply a set of nodes and an associated topology, defined using an isoparametric formulation. The template nodes are added by using their natural coordinates (i.e. the coordinates defined with respect to the template). The position  $x_j$ , in Cartesian coordinates, of the new



node  $j$  is defined as  $\mathbf{x}_j = \mathbf{x}_i \xi_i^j$ , where the Einstein summation convention is applied on the nodes  $i$  of the removed element ( $i = 1, 2, \dots, 8$  for hexahedral elements). The term  $\xi_i^j$  in the interpolating polynomial (known as the shape function in the FEM context) can be seen as the *relative* position of the node  $j$  with respect to the node  $i$ . A two dimensional schematic presentation of the refinement can be seen in Fig. 4. Note that the predefined template is not limited to regular elements, but can be as heterogeneous as desired (i.e. the template with different element sizes). However, to have a good performance in FEM simulation, ill-shaped elements (i.e. elements where one or more edges are much smaller than the largest) should be avoided in defining the template. Note also that we are not limited by the regularity of the mesh, and can start from any (reasonable) heterogeneous mesh as a starting point prior to refinement. Also, using this refinement technique, elements can be refined recursively, see Fig. 4d.

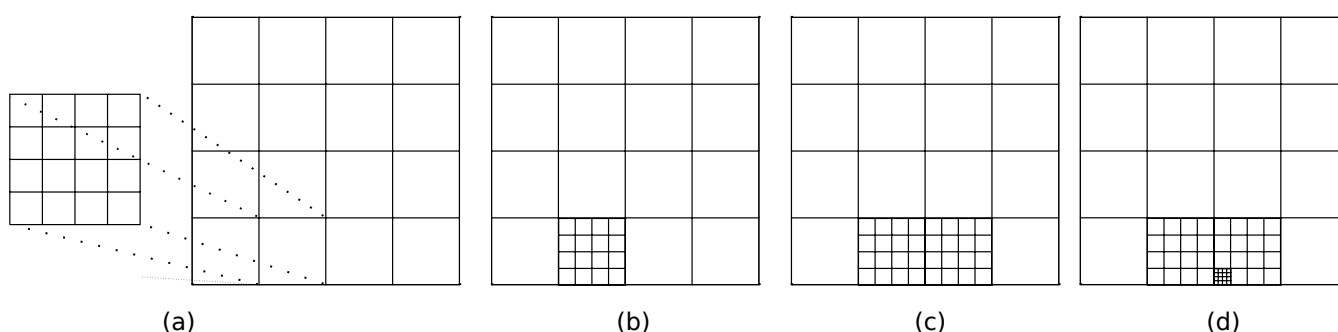


**Figure 4.** Schematic presentation of template-based refinement: (a) A template for refinement can be defined prior to simulation; (b) first element is refined; (c) second element is refined; (d) the refinement can be nested.

Since elements are refined according to the predefined templates, regardless of their neighbourhood, some nonconforming nodes (also known as hanging nodes) are generated. In FEM words, a nonconforming node is a node which is not shared by all elements around it, see Fig. 5. These nodes are also called T-junctions since they form a T-shaped junction in the mesh. Solving the FEM problem without any treatment at T-junctions, displacement discontinuities at these nodes occur. To avoid that, Lagrange multipliers can be used to enforce the continuity at T-junctions, see Section 2.4.

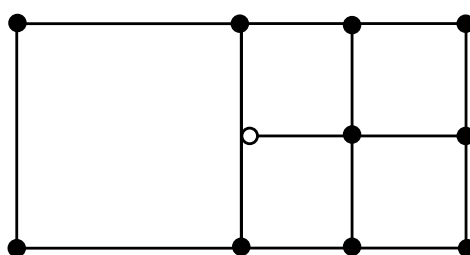


**Figure 5.** Schematic representation of a hanging node (shown by the unfilled circle) in two dimensions.

## 2.4 Solving system equations with constraints

Based on Eq. (13), the interaction between the needle (denoted by subscript 1) and the tissue (denoted by subscript 2) can be expressed by the following equation set

$$\begin{pmatrix} \mathbf{A}_1 & \mathbf{0} & \mathbf{H}_1^T \\ \mathbf{0} & \mathbf{A}_2 & \mathbf{H}_2^T \\ \mathbf{H}_1 & \mathbf{H}_2 & \mathbf{0} \end{pmatrix} \begin{Bmatrix} d\mathbf{v}_1 \\ d\mathbf{v}_2 \\ \lambda_i \end{Bmatrix} = \begin{Bmatrix} \mathbf{b}_1 \\ \mathbf{b}_2 \\ \mathbf{0} \end{Bmatrix}, \quad (17)$$

where  $\lambda_i$  is the Lagrange multiplier representing the *interaction* between the needle and the tissue.

When refinement takes place in the tissue model, T-junctions (as explained above) can be handled by using constraints in the following form

$$\begin{pmatrix} \mathbf{A}_2 & \mathbf{T}^T \\ \mathbf{T} & \mathbf{0} \end{pmatrix} \begin{Bmatrix} d\mathbf{v}_2 \\ \lambda_t \end{Bmatrix} = \begin{Bmatrix} \mathbf{b}_2 \\ \mathbf{0} \end{Bmatrix}. \quad (18)$$

where  $\lambda_t$  stands for Lagrange multipliers used for *T-junctions*, and  $\mathbf{T}$  expresses the dependence between the T-junction nodes (slave nodes) with respect to their parent nodes (master nodes).

We can see that Eqs. (17) and (18) have the same general form

$$\begin{pmatrix} \mathbf{A} & \mathbf{J}^T \\ \mathbf{J} & \mathbf{0} \end{pmatrix} \begin{Bmatrix} \mathbf{x} \\ \lambda \end{Bmatrix} = \begin{Bmatrix} \mathbf{b} \\ \mathbf{0} \end{Bmatrix}. \quad (19)$$

Eq. (19) can be reformulated as

$$\mathbf{x} = \underbrace{\mathbf{A}^{-1}\mathbf{b}}_{\mathbf{x}_{free}} - \mathbf{A}^{-1}\mathbf{J}^T\lambda, \quad (20a)$$

$$\mathbf{J}\mathbf{A}^{-1}\mathbf{J}^T\lambda = \mathbf{J}\underbrace{\mathbf{A}^{-1}\mathbf{b}}_{\mathbf{x}_{free}}, \quad (20b)$$

in which,  $\mathbf{x}_{free}$  can be seen as the solution of the unconstrained system  $\mathbf{A}\mathbf{x} = \mathbf{b}$ . Therefore, Eq. (19) can be solved in three steps as

- Step 1. Factorize the matrix  $\mathbf{A}$  to have its inverse  $\mathbf{A}^{-1}$ , and solve for  $\mathbf{x}_{free}$ ,
- Step 2. Solve Lagrange multipliers  $\lambda$  from Eq. (20b),
- Step 3. Once  $\lambda$  is available,  $\mathbf{x}$  can be obtained from Eq. (20a) by using  $\mathbf{x}_{free}$ .

## 3 RESULTS

To demonstrate the efficiency of our method, we present several numerical studies. To show the benefits of employing adaptive refinement controlled by error estimates, we first study the simulation of needle insertion into a phantom tissue of simple geometry. Then, we study a more complex simulation of deep-brain stimulation (DBS) lead insertion. In DBS, a cannula is inserted into the brain tissue in order to reach an STN target. Leaving an electrode inside the brain, the cannula is then pulled back until completely outside of the brain. By these studies, we provide insight into the mechanical behaviour of the brain tissue in response to the lead insertion, and analyse the effect of mesh adaptivity on the solution.

DBS is an effective approach to alleviate the symptoms of neuro-degenerative diseases such as Parkinson's disease. During most DBS interventions, the craniotomy leads to a shift of the brain within the skull, because of the cerebrospinal fluid which is drained out of the skull cavity and ceases to provide buoyancy to the brain. Once the electrode has been inserted, the brain regains its original position.

One of the difficulties during DBS interventions is that the electrode displaces as the brain comes back to its original position, before brain shift. Therefore, it is possible that the electrode tip displaces, so that the electrode does not stimulate the proper target anymore, which requires a new operation.

Simulations of the type that we are presenting here have the potential to help surgeons prepare for interventions by investigating where the electrode tip should be located, so that it stimulates the target *after the brain shifts back to the configuration it had prior to craniotomy-induced brain shift*.

### 3.1 Impact of local mesh refinement on displacement field

In order to exhibit the effect of the adaptive refinement on a trade-off between computational time and precision, a needle insertion simulation into a phantom tissue test is carried out, see Fig. 6. For this study, we consider the Young's modulus of 50 MPa for the needle, and 10 MPa for the tissue, whereas the Poisson's ratio is taken as 0.4 for the tissue, and 0.3 for the needle, respectively. It is noted that, for this heuristic study, these parameters are chosen arbitrarily (but are physically meaningful for a needle-tissue interaction problem).

As mentioned above, a linear elastic model based on corotational formulation is employed for the needle as well as the tissue. The dimension of the tissue is  $4 \times 2 \times 2$  cm. The needle length and radius are of 3.2 cm and 0.1 cm, respectively.

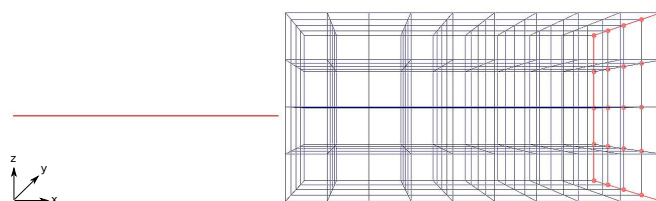


**Figure 6.** Schematic representation of needle insertion simulation into a phantom tissue. The phantom tissue is clamped at the right surface.

The mesh is subsequently refined in a uniform manner ( $8 \times 4 \times 4$ ,  $16 \times 8 \times 8$ ,  $32 \times 16 \times 16$  elements), as well as in an adaptive manner (starting with the coarse mesh  $8 \times 4 \times 4$  nodes and adaptively refining the mesh during the simulation). Within the adaptive meshing scheme, the mesh refinement is guided by the error estimate described in Section 2. During needle insertion, we measure the displacement of the points defined in Fig. 7.

Note that the displacements of all points is not shown here. Fig. 8 shows the displacement of some points distributed in the direction of the needle shaft, and Fig. 9 shows the displacement of some points distributed in the direction normal to the needle shaft (i.e. radial). These results reveal two distinct features. Firstly, the displacement solution of the adaptive refinement scheme agrees well with that of fine mesh when the adaptivity criterion is appropriately chosen (here  $\theta = 0.3$ ). Secondly, it is observed that after puncture, the finer the mesh is used, the smaller the displacements at those points are. This observation is explained by two phenomena. First, a finer mesh produces softer behaviour for the tissue, i.e. the displacement does not “propagate” as easily from the needle shaft to the point where we measure the displacement (refer to

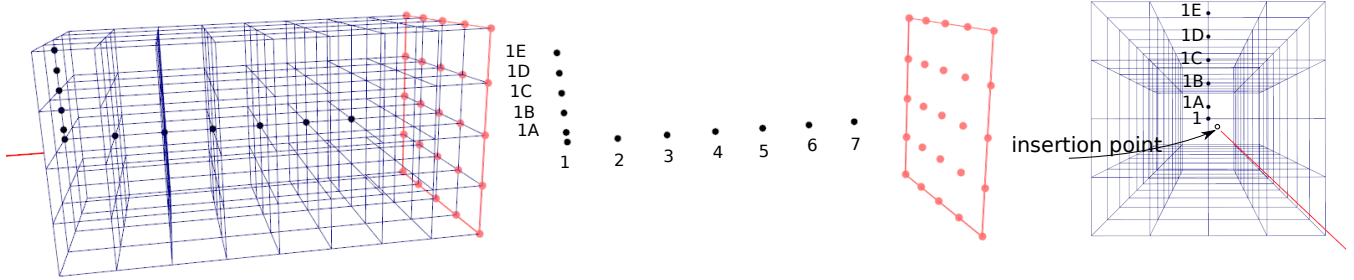


**Figure 7.** The displacement during insertion is measured at the predefined points, namely, 1, 2, 3, 4, 5, 6, 7 which are distributed in the direction of the needle shaft, and 1A, 1B, 1C, 1D, 1E that lie in the direction normal to the needle shaft.

Bui et al. (2016) for details). Second, needle insertion leads to localisation of displacements, strains and stresses, due to the small size of the needle compared to the organ.

Fig. 10 shows the displacement at all predefined points during insertion when mesh  $32 \times 16 \times 16$  is employed. It is seen that the further the point from the tissue surface is (Fig. 10a), or the further the point from the needle shaft is (Fig. 10b), the smaller the displacement of that point is. The physical relevance of this observation is explained in the previous paragraph.

### 3.2 Electrode implantation in DBS

We study the simulation of DBS lead placement by inserting a cannula into a brain model until it reaches the predefined STN target. Then, the cannula is retracted while keeping an electrode inside the brain. As in Bilger et al. (2011), for this study we consider the Young's modulus of 10 GPa for the cannula and the electrode, and 6 kPa for the brain tissue, whereas the Poisson's ratio is taken as 0.45 for the brain tissue and 0.3 for both the cannula and electrode. The radii of the cross sections are set to 3 mm and 0.7 mm for the cannula and electrode, respectively. The friction coefficient between the cannula and the brain tissue is set to 0.05. The adaptivity parameter  $\theta$  is set to 0.6. From our studies, we found that, with minimum DOFs, this choice of the adaptivity parameter gives the best results for DBS simulation of electrode placement. Since the brain tissue is very soft, we set the penetration strength at the brain surface and the cutting strength to 0.01 N.

It is worth mentioning that, in this study, simple boundary conditions around the brain tissue are taken into account. Indeed, only fixed bilateral constraints near the area of the optic nerves and the brainstem are considered. We believe that this choice of boundary conditions (for the sake of simplicity) does not affect the efficiency of the adaptive refinement algorithm. However, more complex boundary conditions for the brain with respect to the skull can be found in Wittek et al. (2007), Bilger et al. (2011). We are currently investigating the effects of the choice of boundary conditions on the results for this particular case. In general, for brain shift problems, it is now known that the type of boundary conditions does not have a strong effect on the resulted brain shift, see, e.g., Wittek et al. (2005), Joldes et al. (2009). However, systematic studies are still missing from the literature for the problem of DBS simulation.

Two types of mesh refinement are employed. The first one, called uniform refinement, consists of subsequently refining every hexahedral element into 8 smaller elements. In the second approach, called adaptive refinement, only those elements that fulfil the adaptivity condition Eq. (16), are refined.

In Fig. 11, brain shift prior to insertion is shown. Fig. 12 shows the distance between the electrode tip and the STN target during insertion and retraction of the cannula. The vertical line in Fig. 12 indicates

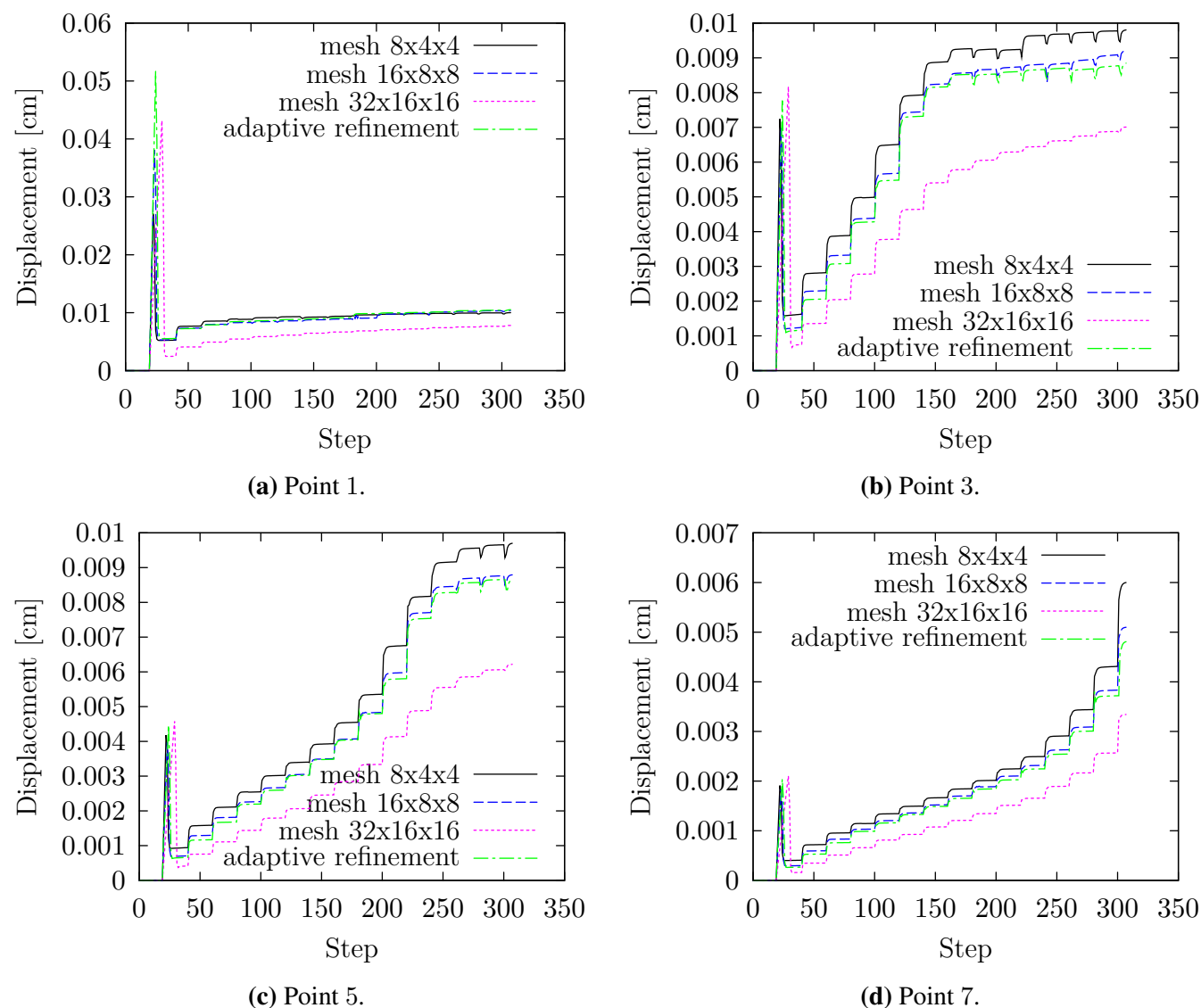


**Figure 8.** During needle insertion, the displacement of the points located in the direction of the needle shaft, uniform and adaptive refinement schemes. The numbers of degrees of freedom for the meshes listed in the graphs (in the label order) are 675, 4 131, 28 611, and 1 461 (for adaptive refinement scheme it is the maximum at the end of insertion step). It is seen that the displacement solution of adaptive refinement scheme agrees well with that of fine mesh when certain criterion of adaptivity is appropriately chosen (here  $\theta = 0.3$ ). Moreover, it is observed that the finer the mesh is used, the smaller the displacements at those points are.

the point in time when the cannula has the trend to be pulled back. It is observed that from that time, the distance between the electrode tip and the STN target still decreases. This is justified by the fact that the brain tissue is unloaded from insertion forces and displaces toward the direction from which the needle was inserted. The electrode, on the other hand keeps moving forward due to inertial forces. When the cannula is being retracted, the brain tissue deforms and moves backward, and thus increases the electrode-STN target distance accordingly. When the cannula is completely outside the brain tissue, that distance is stabilised at around 2.9 mm.

Moreover, Fig. 12 reveals that the distance from the electrode tip to the STN target obtained by using our adaptive refinement scheme agrees well with that when a fine uniform mesh is employed. However,

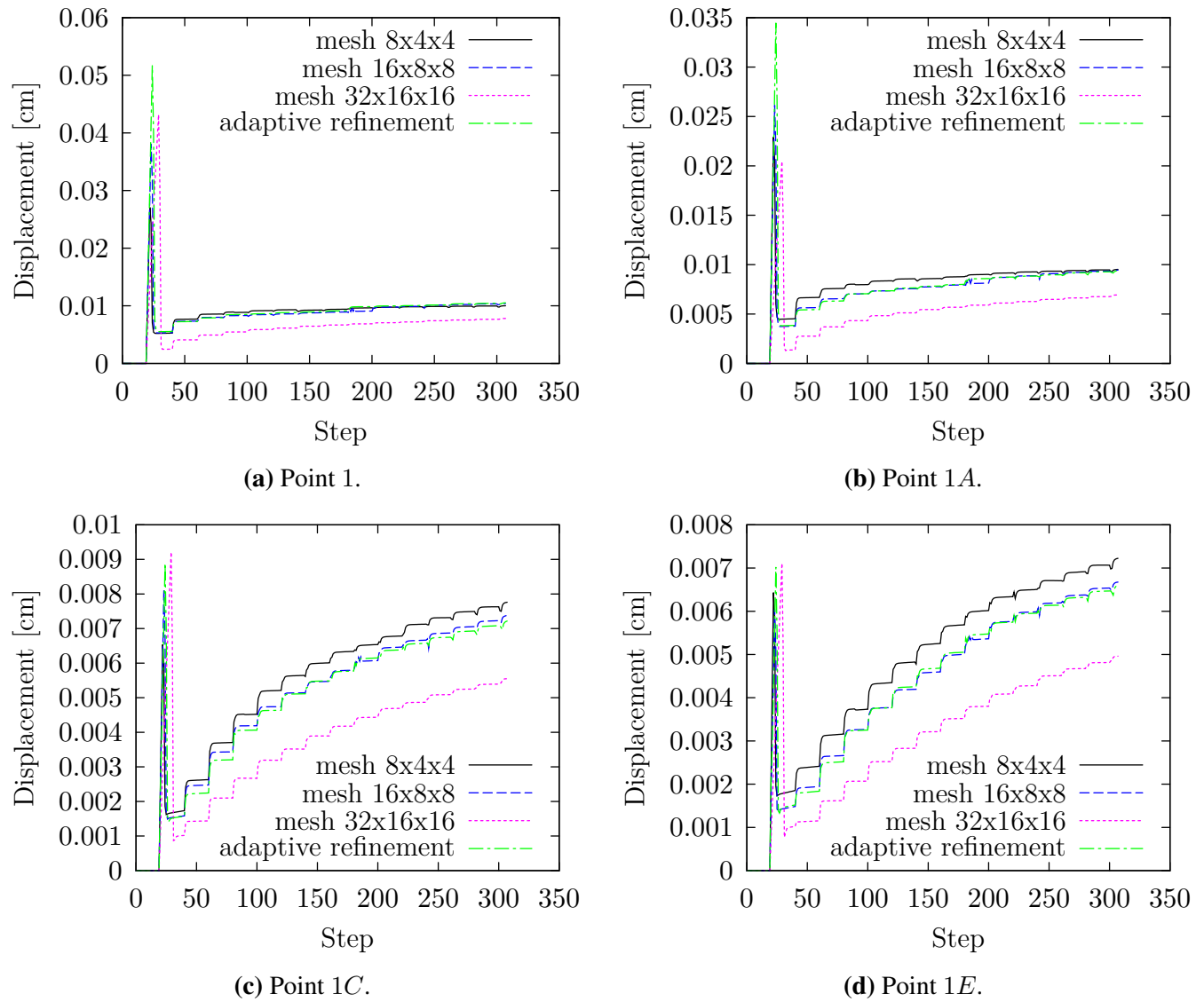


**Figure 9.** The displacement of the points located in the radial direction, uniform and adaptive refinement schemes, during needle insertion. The numbers of degrees of freedom for the meshes listed in the graphs (in the label order) are 675, 4 131, 28 611, and 1 461 (for adaptive refinement scheme it is the maximum at the end of insertion step). The same observations can be made as in Fig. 8.

an important gain in computational time can be observed, since the maximum number of DOFs for the adaptive scenario is only 3 135 as compared to 12 528 DOFs of the fine uniform mesh. This reduction in the problem size is approximately of the order of 4.

Fig. 13 shows the displacement of the STN target (with respect to its position after brain shift) when inserting the cannula, leaving the electrode, and retracting the cannula. It can be seen that at around the step 75, the cannula starts penetrating into the brain tissue, and thus provokes the displacement of the STN target inside the brain. This displacement increases along with the insertion of the cannula and the electrode into the brain, due to cutting of the brain tissue and friction on the cannula shaft. At the step 166, when the cannula starts undergoing retraction, the brain tissue is then unloaded, and this causes the STN target to move backward. This phenomenon is seen by the decrease of the STN target displacement up to the step between 200 and around 225 (depending on the mesh employed, refer to Fig. 13). After that, since the

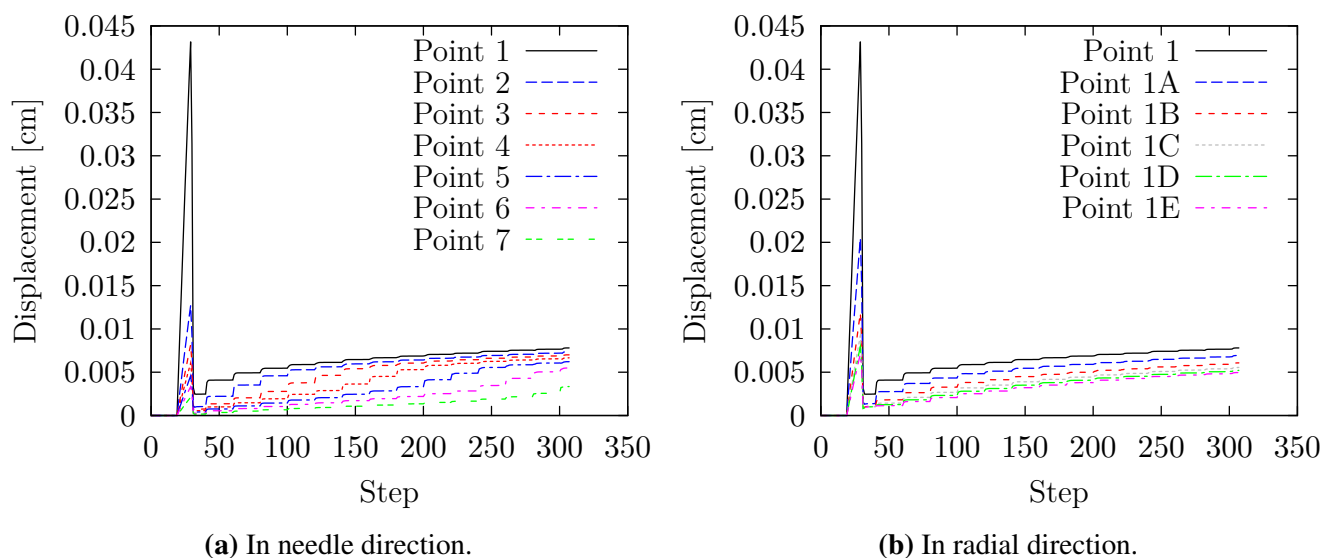


**Figure 10.** Displacement of the points during needle insertion, when the  $32 \times 16 \times 16$  mesh is employed. The further the point from the tissue surface, or from the needle shaft, is found, the smaller the displacement of that point is.

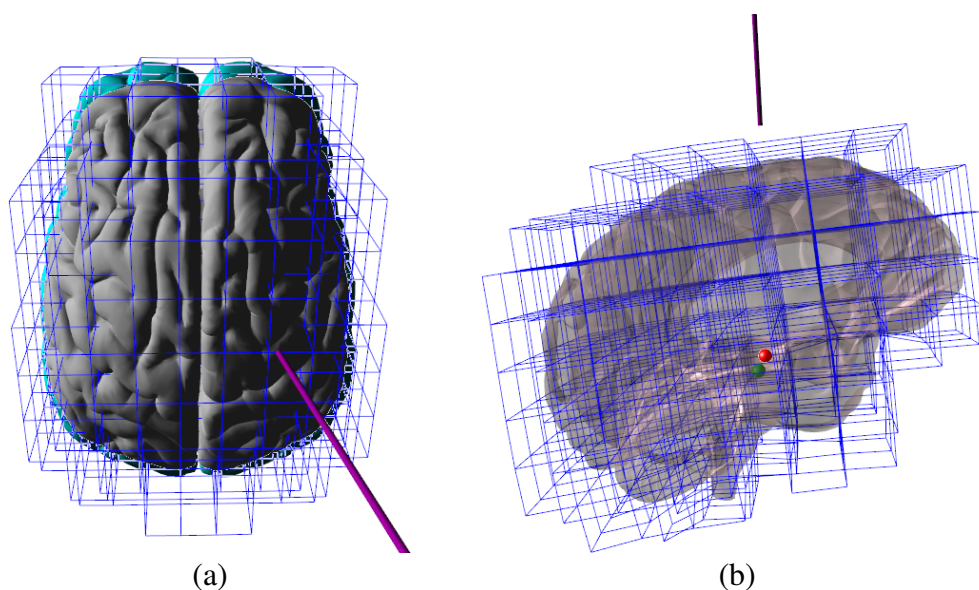


**Figure 11.** Simulation of brain shift prior to insertion of the cannula for electrode implantation. Initial position of the brain is shown by cyan colour (a). The position of the STN target after brain shift is shown by the green sphere, while its initial position is shown by the red one (b). The displacement of the STN target due to brain shift is about 6.5 mm.

cannula is bearing retraction, and because of friction, the brain tissue follows the cannula in the direction of the retraction. As a consequence, the displacement of the STN target increases again. The closer to the brain surface the cannula tip is, the smaller the magnitude of frictional force along the cannula shaft is, and therefore, at some stage, the STN target displacement decreases again. And, that displacement continuously decreases when the cannula is fully retracted from the brain tissue, as observed at the final stage of Fig. 13.

Visualisation of the simulation of DBS lead implantation during insertion and retraction at some stages can be seen in Fig. 14. Fig. 13 reveals that, during the insertion phase, the result of the adaptive mesh does



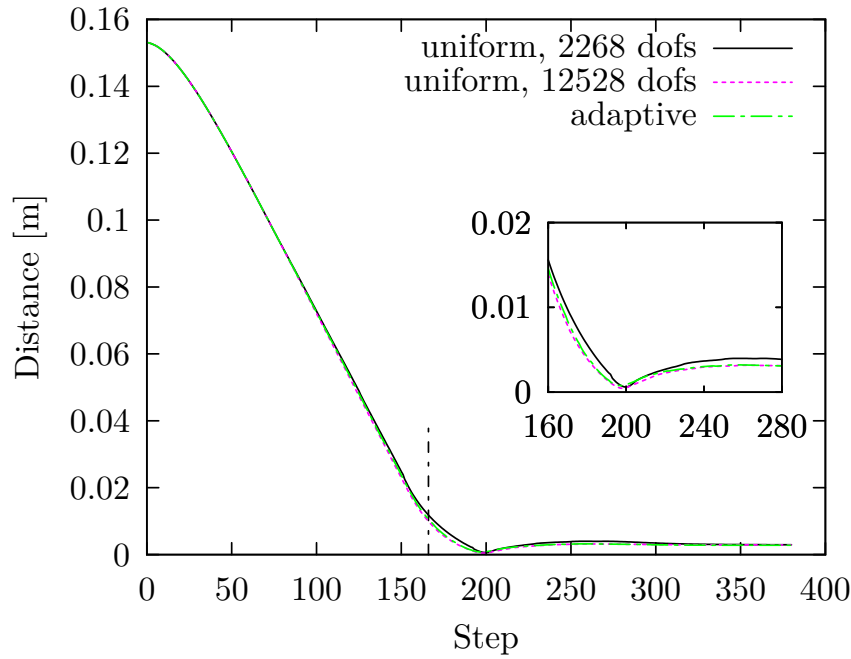


**Figure 12.** The distance from the electrode tip to the STN target. An STN target is fixed inside the brain. The cannula is inserted into the brain so that it can reach the STN target. Then the electrode is left while retracting the cannula. The vertical line at step 166 indicates the moment when the cannula has the trend to be pulled back. It is seen that using an adaptive refinement scheme, the distance obtained between the electrode tip and the STN target is as good as using the fine uniform mesh. However, a significant gain in computational time is observed. The maximum number of degrees of freedom for the adaptive refinement is 3,135. For a similar solution profile, compared to a uniformly refined mesh, this represents a reduction in the problem size of approximately 4.

not closely agree with that of the uniform fine mesh. This is evidenced by the fact that the refinement has begun but has not reached the STN target yet, as can be partly seen in Fig. 14b. However, from the stage when the cannula reaches the STN target, to the end of the simulation when it is completely pulled out of the brain tissue, the result of the adaptive mesh agrees well with that of the uniform fine mesh, thanks to the refinement occurring along the cannula trajectory, as seen in Fig. 14d.

It is again observed that the use of the proposed adaptive refinement scheme is very relevant because it guarantees the solution accuracy close to the fine meshing schemes, with computational time suitable for real-time simulation.

## 4 CONCLUSIONS

We presented a structured approach to answering the crucial, but rarely tackled, question of accuracy in surgical simulation. The novelty of our paper is the use of an a posteriori estimate of the discretisation error to automatically drive local adaptive mesh refinement during needle insertion.

From the study on the displacement solution of two different problems (needle insertion into a simple phantom geometry with stiff mechanical properties, and the simulation of electrode implantation for deep brain stimulation (DBS) with softer mechanical properties for the brain), two major conclusions can be drawn:

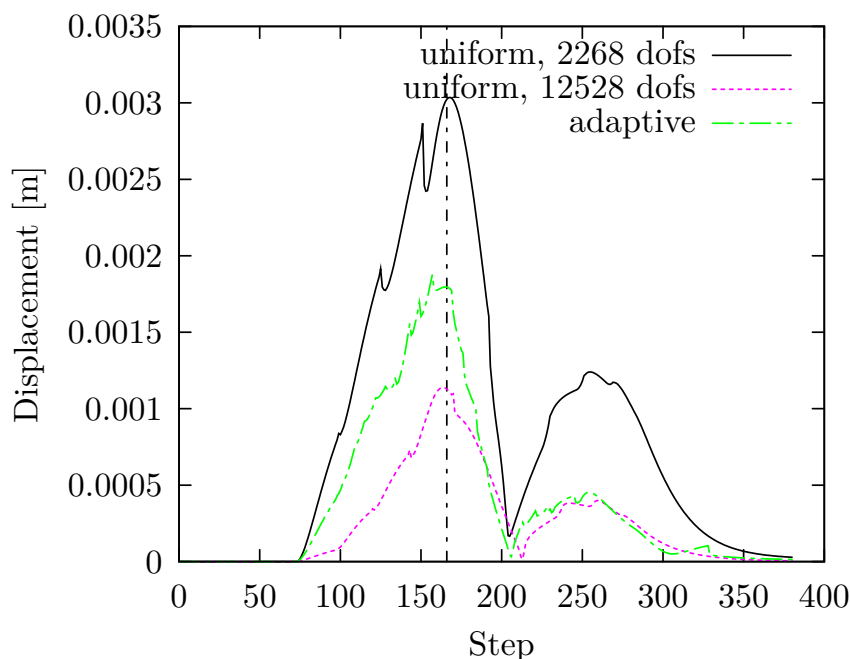


**Figure 13.** Displacement of STN target (with respect to its position after brain shift) during cannula insertion and retraction (the same simulations as in Fig. 12). The vertical line, same as in Fig. 12, shows the stage when the cannula is going to be removed. The maximum number of DOFs for the adaptive refinement is 3135.

- The outcome of the proposed adaptive refinement scheme does not depend on the mechanical parameters of the tissue, such as Young's modulus and Poisson's ratio.
- With a suitably chosen refinement criterion, the adaptive solution agrees well with the solution on a fine uniform mesh, while saving computational time to make it feasible for real-time simulations. The computational time savings in the particular case we tackled are of the order of 10 (more details can be found in Bui et al. (2016)).

Our work is limited in several ways which we are currently investigating:

- We tackled only the discretisation error, and avoided the difficult problem of “model error”. For example, we assumed the brain to behave in a corotational manner. Although this is corroborated by the literature, we do not have physical evidence that this assumption is true in general, nor as to when it may break down.
- We assumed simple boundary conditions around the brain. This should be investigated in more detail to assess the effect of both geometrical and boundary condition uncertainty on the outcome of the simulations.
- Soft tissue properties vary from patient to patient by up to a few orders of magnitude. We have been working on robust and systematic approaches to quantifying these uncertainties (Hauseux et al., 2017). We will use these methods to quantify the effects of variability in the material parameters on the motion of the target and of the electrode during DBS.

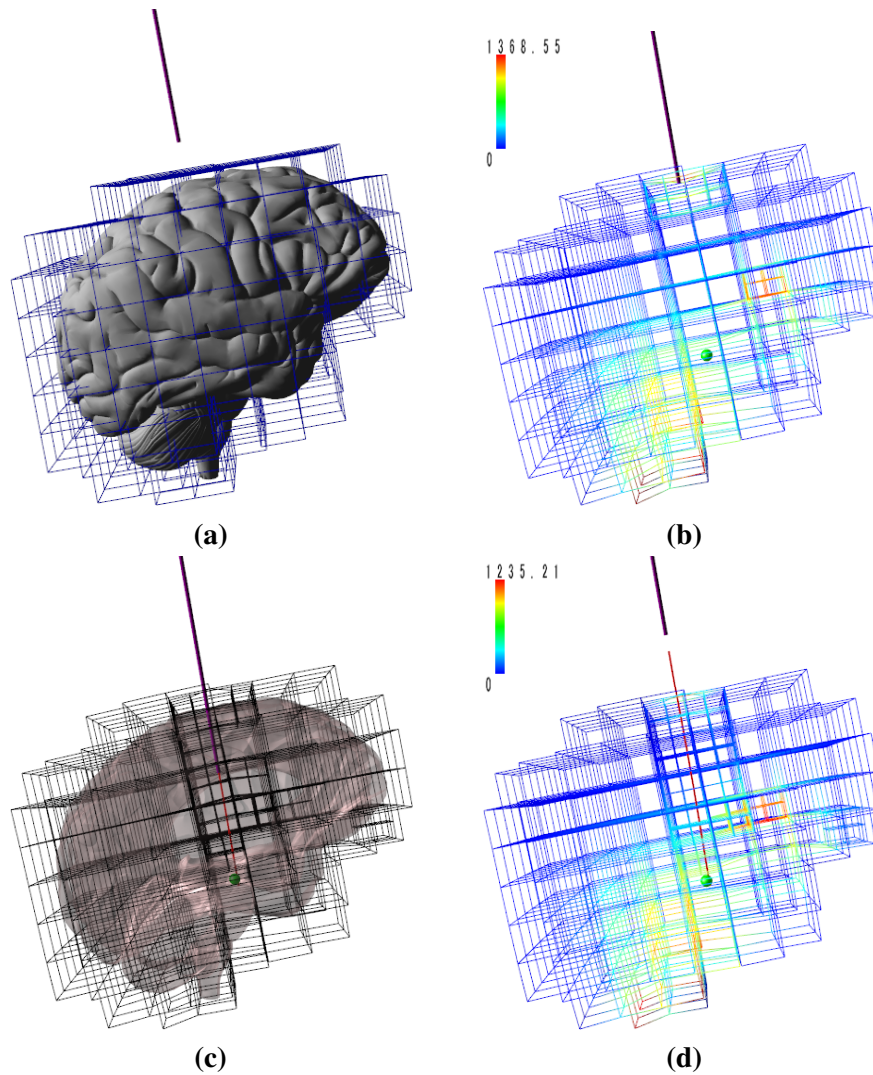


**Figure 14.** Visualisation of the electrode implantation simulation of DBS (a). Brain shift occurs prior to cannula insertion. The STN target during the simulation is shown at different stages by a green sphere in (b,c,d). When the cannula tip is in contact with the brain tissue surface, it leads to element refinement guided by error estimate, shown in (b), coloured by Von Mises stress magnitude. When the cannula has reached the STN target, it undergoes a retraction. The cannula is being retracted while the electrode is left inside the brain, shown in (c). The cannula is completely retracted, adaptive refinement has occurred along the trajectory of the cannula, shown in (d).

## ACKNOWLEDGMENTS

Stéphane Bordas, Satyendra Tomar and Huu Phuoc Bui thank partial funding for their time provided by the European Research Council Starting Independent Research Grant (ERC Stg grant agreement No. 279578) RealTCut “Towards real time multiscale simulation of cutting in non-linear materials with applications to surgical simulation and computer guided surgery”. We also also grateful for the funding from the Luxembourg National Research Fund (INTER/MOBILITY/14/8813215/CBM/Bordas and INTER/FWO/15/10318764).

Inria thanks for funding of European project RASimAs (FP7 ICT-2013.5.2 No. 610425).

The funding from the University of Strasbourg Institute for Advanced Study (BPC 14/Arc 10138) for the first author is gratefully acknowledged.

Huu Phuoc Bui thanks Dr. Davide Baroli and Mr. Vahid Shahrabi for their useful helps about PyMesh (<https://github.com/qnzhou/PyMesh>) and Meshmixer (<http://www.meshmixer.com>).

The authors would also like to thank Dr. Alexandre Bilger and Mr. Rémi Bessard Duparc for their general helps.

## REFERENCES

- Abolhassani, N., Patel, R., and Moallem, M. (2007). Needle insertion into soft tissue: A survey. *Medical Engineering and Physics* 29, 413–431
- Alterovitz, R., Goldberg, K., and Okamura, A. (2005). Planning for steerable bevel-tip needle insertion through 2d soft tissue with obstacles. In *Proceedings of ICRA 2005*. 1652–1657
- Baraff, D. and Witkin, A. (1998). Large steps in cloth simulation. In *Proceedings of SIGGRAPH*. 43–54
- Bartels, S. and Carstensen, C. (2002). Each averaging technique yields reliable a posteriori error control in FEM on unstructured grids. II. Higher order FEM. *Math. Comp.* 71, 971–994 (electronic). doi:10.1090/S0025-5718-02-01412-6
- Belytschko, T., Parimi, C., Moës, N., Sukumar, N., and Usui, S. (2003). Structured extended finite element methods for solids defined by implicit surfaces. *International Journal for Numerical Methods in Engineering* 56, 609–635. doi:10.1002/nme.686
- Bilger, A., Dequidt, J., Duriez, C., and Cotin, S. (2011). *Biomechanical Simulation of Electrode Migration for Deep Brain Stimulation* (Berlin, Heidelberg: Springer Berlin Heidelberg). 339–346. doi:10.1007/978-3-642-23623-5\_43
- Bordas, S., Duflot, M., and Le, P. (2008). A simple error estimator for extended finite elements. *Communications in Numerical Methods in Engineering* 24, 961–971. doi:10.1002/cnm.1001
- Breit, S., Schulz, J. B., and Benabid, A.-L. (2004). Deep brain stimulation. *Cell and Tissue Research* 318, 275–288. doi:10.1007/s00441-004-0936-0
- Bui, H. P., Tomar, S., Courtecuisse, H., Cotin, S., and Bordas, S. P. A. (2016). Real-time error control for surgical simulation. *Accepted for publication in IEEE Transactions on Biomedical Engineering* <http://hdl.handle.net/10993/28624> and <http://arxiv.org/abs/1610.02570>
- Burman, E., Claus, S., Hansbo, P., Larson, M. G., and Massing, A. (2015). Cutfem: Discretizing geometry and partial differential equations. *International Journal for Numerical Methods in Engineering* 104, 472–501. doi:10.1002/nme.4823
- Calabrese, E. (2016). Diffusion Tractography in Deep Brain Stimulation Surgery: A Review. *Frontiers in Neuroanatomy* 10, 45. doi:10.3389/fnana.2016.00045
- Carstensen, C. and Bartels, S. (2002). Each averaging technique yields reliable a posteriori error control in FEM on unstructured grids. I. Low order conforming, nonconforming, and mixed FEM. *Math. Comp.* 71, 945–969 (electronic). doi:10.1090/S0025-5718-02-01402-3
- Courtecuisse, H., Allard, J., Kerfriden, P., Bordas, S. P., Cotin, S., and Duriez, C. (2014). Real-time simulation of contact and cutting of heterogeneous soft-tissues. *Medical Image Analysis* 18, 394 – 410
- Dehghan, E., Wen, X., Zahriri-Azar, R., Marchal, M., and Salcudean, S. (2008). Needle-tissue interaction modeling using ultrasound-based motion estimation: Phantom study. *Computer Aided Surgery* 13, 265–280
- DiMaio, S. and Salcudean, S. (2003). Needle insertion modeling and simulation. *IEEE Transactions on Robotic Automation* 19, 864–875

- Duriez, C., Guébert, C., Marchal, M., Cotin, S., and Grisoni, L. (2009). Interactive simulation of flexible needle insertions based on constraint models. In *Lecture Notes in Computer Science*. vol. 5762, 291–299
- Elgezua, I., Kobayashi, Y., and Fujie, M. G. (2013). Survey on current state-of-the-art in needle insertion robots: Open challenges for application in real surgery. In *Procedia CIRP*. vol. 5. doi:10.1016/j.procir.2013.01.019
- Felippa, C. and Haugen, B. (2005). A unified formulation of small-strain corotational finite elements: I. theory. *Computer Methods in Applied Mechanics and Engineering* 194, 2285 – 2335
- Griebel, M. and Schweitzer, M. A. (2003). *Meshfree Methods for Partial Differential Equations* (Springer-Verlag Berlin Heidelberg)
- Hamzé, N., Peterlík, I., Cotin, S., and Essert, C. (2016). Preoperative trajectory planning for percutaneous procedures in deformable environments. *Computerized Medical Imaging and Graphics* 47, 16–28
- Hamzé, N., Bilger, A., Duriez, C., Cotin, S., and Essert, C. (2015). Anticipation of brain shift in deep brain stimulation automatic planning. In *2015 37th Annual International Conference of the IEEE Engineering in Medicine and Biology Society (EMBC)*. 3635–3638. doi:10.1109/EMBC.2015.7319180
- Hauseux, P., Hale, J. S., and Bordas, S. P. (2017). Accelerating monte carlo estimation with derivatives of high-level finite element models. *Computer Methods in Applied Mechanics and Engineering* , –doi:http://dx.doi.org/10.1016/j.cma.2017.01.041
- Heverly, M., Dupont, P., and Triedman, J. K. (2005). Trajectory Optimization for Dynamic Needle Insertion. In *ICRA (IEEE)*, 1646–1651
- Hing, J. T., Brooks, A. D., and Desai, J. P. (2006). Reality-based needle insertion simulation for haptic feedback in prostate brachytherapy. In *Proceedings 2006 IEEE International Conference on Robotics and Automation, 2006. ICRA 2006*. 619–624. doi:10.1109/ROBOT.2006.1641779
- Jiang, S., Hata, N., and Kikinis, R. (2008). Needle insertion simulation for image-guided brachytherapy of prostate cancer. In *2008 2nd International Conference on Bioinformatics and Biomedical Engineering*. 1682–1685. doi:10.1109/ICBBE.2008.749
- Joldes, G. R., Wittek, A., and Miller, K. (2009). Computation of intra-operative brain shift using dynamic relaxation. *Computer Methods in Applied Mechanics and Engineering* 198, 3313 – 3320. doi:http://doi.org/10.1016/j.cma.2009.06.012
- Lee, C.-K., Mihai, L. A., Hale, J. S., Kerfriden, P., and Bordas, S. P. (2017). Strain smoothing for compressible and nearly-incompressible finite elasticity. *Computers & Structures* 182, 540 – 555. doi:http://doi.org/10.1016/j.compstruc.2016.05.004
- Liu, G. R. and Quek, S. S. (2014). Chapter 3 - Fundamentals for Finite Element Method. In *The Finite Element Method (Second Edition)*, eds. G. R. Liu, , and S. S. Quek (Oxford: Butterworth-Heinemann). Second edition edn., 43–79. doi:http://dx.doi.org/10.1016/B978-0-08-098356-1.00003-5
- Mahvash, M. and Dupont, P. E. (2009). Fast Needle Insertion to Minimize Tissue Deformation and Damage. In *Proceedings of the 2009 IEEE International Conference on Robotics and Automation* (Piscataway, NJ, USA: IEEE Press), ICRA'09, 2761–2766
- Mendizabal, A., Bessard Duparc, R., Bui, H. P., Paulus, C. J., Peterlik, I., and Cotin, S. (2017). Face-based smoothed finite element method for real-time simulation of soft tissue. doi:10.1117/12.2255064
- Mihai, L. A., Chin, L., Janmey, P. A., and Goriely, A. (2015). A comparison of hyperelastic constitutive models applicable to brain and fat tissues. *Journal of The Royal Society Interface* 12. doi:10.1098/rsif.2015.0486
- Misra, S., Reed, K., Schafer, B., Ramesh, K., and Okamura, A. (2010). Mechanics of flexible needles robotically steered through soft tissue. *Int. J. Rob. Res.* 29, 1640–1660



- Nealen, A., Müller, M., Keiser, R., Boxerman, E., and Carlson, M. (2006). Physically based deformable models in computer graphics. In *Computer graphics forum*. vol. 25, 809–836
- Nguyen, V. P., Rabczuk, T., Bordas, S., and Duflot, M. (2008). Meshless methods: a review and computer implementation aspects. *Mathematics and computers in simulation* 79, 763–813
- Nguyen-Xuan, H., Rabczuk, T., Nguyen-Thanh, N., Nguyen-Thoi, T., and Bordas, S. (2010). A node-based smoothed finite element method with stabilized discrete shear gap technique for analysis of reissner–mindlin plates. *Computational Mechanics* 46, 679–701. doi:10.1007/s00466-010-0509-x
- Piasecki, S. D. and Jefferson, J. W. (2004). Psychiatric complications of deep brain stimulation for parkinson’s disease. *The Journal of clinical psychiatry* 65, 845–849
- Pinelli, A., Naqavi, I. Z., Piomelli, U., and Favier, J. (2010). Immersed boundary method for generalised finite volume and finite difference navier-stokes solvers. *Journal of Computational Physics* 229, 9073–9091
- Tang, L., chen, Y., and He, X. (2008). Compliant needle modeling and steerable insertion simulation. *Computer-Aided Desing and Applications* 5, 39–46
- Wang, Y., Jacobson, A., Barbič, J., and Kavan, L. (2015). Linear subspace design for real-time shape deformation. *ACM Transactions on Graphics (TOG)* 34, 57
- Watkins, D. S. (2005). *Fundamentals of Matrix Computations* (John Wiley & Sons, Inc.). doi:10.1002/0471249718.ch1
- Webster, R., Kim, J., Cowan, N., Chirikjian, G., and Okamura, A. (2006). Nonholonomic modeling of needle steering. *International Journal of Robotics Research* 5, 509–525
- Witte, A., Kikinis, R., Warfield, S. K., and Miller, K. (2005). *Brain Shift Computation Using a Fully Nonlinear Biomechanical Model* (Berlin, Heidelberg: Springer Berlin Heidelberg). 583–590. doi:10.1007/11566489\_72
- Witte, A., Miller, K., Kikinis, R., and Warfield, S. (2007). Patient-specific model of brain deformation: Application to medical image registration. *Journal of biomechanics*
- Wu, X., Downes, M. S., Goktekin, T., and Tendick, F. (2001). Adaptive nonlinear finite elements for deformable body simulation using dynamic progressive meshes. *Computer Graphics Forum* 20, 349–358. doi:10.1111/1467-8659.00527
- Zienkiewicz, O. and Taylor, R. (2000). *The Finite Element Method: Solid mechanics*. Referex collection.Mecánica y materiales (Butterworth-Heinemann)
- Zienkiewicz, O., Taylor, R., and Zhu, J. (2013). *The finite element method: Its basis and fundamentals*, vol. 1 (Elsevier)
- Zienkiewicz, O. and Zhu, J. (1992). The superconvergent patch recovery (SPR) and adaptive finite element refinement. *Computer Methods in Applied Mechanics and Engineering* 101, 207–224